Check for updates

Broad-range spin-crossover modulation in guest-responsive 2D Hofmann-type coordination polymers†

Alejandro Orellana-Silla, ‡[a] Rubén Turo-Cortés, [iD] ‡[a] Víctor Rubio-Giménez, [iD] [b] Carlos Bartual-Murgui, [iD] *[a] Rob Ameloot, [iD] [b] Carlos Martí-Gastaldo, [iD] [a] M. Carmen Muñoz [iD] [c] and José Antonio Real [iD] *[a]

Rationalizing the role of chemical functionalisation in the synergy between spin crossover (SCO) and guest adsorption properties in porous Fe^{II} coordination polymers is a central topic in the switchable materials field. However, obtaining meaningful magneto-structural information requires the comparison between structural platforms whose topology remains unaltered upon chemical function exchange. Here, based on the previously reported SCO two-dimensional Hofmann-type compounds {Fe(NH₂Pym)₂[M(CN)₄]}·xguest (**1(NH₂)^M·xguest**; 5-NH₂Pym = 5-aminopyrimidine; M = Pd^{II}, Pt^{II}; guest = H_2O, MeOH, EtOH; x = 0–1), we present the isostructural networks **1(OH)^M·xguest** resulting from the replacement of the 5-NH₂Pym axial ligand with 5-OHPym (5-hydroxipryrimidine). The evaluation of their temperature-dependent magnetic and calorimetric data reveals that whereas the unsolvated counterparts (**1(NH₂)^M** and **1(OH)^M**) undergo complete one step spin transitions with small variations in their SCO temperatures (T_c), the solvated species markedly differ not only in T_c but also in the shape of the spin transition curve. A relevant example is observed for **1(NH₂)^M·0.5MeOH** and **1(OH)^M·0.5MeOH**, which present incomplete one-step and complete three-step spin transitions, respectively. These changes are also complementary to the higher adsorption capacities of the hydroxy-functionalised compounds according to the guest uptake isotherms, powder X-ray diffraction and thermogravimetric data. The single crystal-to-single crystal transformations occurring upon the sorption–desorption of guest molecules have permitted us to determine the structural reasons explaining the variation of the SCO and adsorption properties with chemical functionalisation.

ᵃInstituto de Ciencia Molecular/Departamento de Química Inorgánica, Universitat de València, Catedrático José Beltrán Martínez 2, E-46980 Paterna, Valencia, Spain. E-mail: carlos.bartual@uv.es, jose.a.real@uv.es
ᵇCentre for Membrane Separations, Adsorption, Catalysis and Spectroscopy (cMACS), Katholieke Universiteit Leuven, Celestijnenlaan 200F, 3001 Leuven, Belgium
ᶜDepartamento de Física Aplicada, Universitat Politècnica de València, Camino de Vera S/N, 46022 Valencia, Spain

Introduction

Molecular materials with switching properties are relevant research targets of great interest due to their potential for implementation in functional sensors and devices.[1–6] In particular, spin crossover (SCO) metal complexes constitute some of the most important platforms of switching molecular

materials. These complexes, made up essentially of octahedrally coordinated $3d^4$–$3d^7$ metal centres, reversibly change between high-spin (HS) and low-spin (LS) electronic states in response to stimuli such as temperature and pressure gradients, light irradiation, and uptake of specific guests.[7–9]

The most important source of SCO belongs to the chemistry of Fe^{II}-based octahedral systems ($3d^6$).[10–15] In these complexes, the HS ($t_{2g}^4 e_g^2$) ↔ LS ($t_{2g}^6 e_g^0$) switch is accompanied by a complete depopulation/population of the e_g orbitals that involves a shortening/lengthening of the average ⟨Fe–N⟩ bond length of about 0.2 Å. This electron–phonon coupling affords, in the case of extended networks (*i.e.* coordination polymers),[1,16] coherent intermolecular interactions which are an important source of cooperative phenomena,[17] *i.e.* hysteretic behaviour (memory effect), multistability and phase transitions that are perfectly reflected in the magnetic, optical, dielectric and structural properties of a SCO material.[18–22]

An archetype platform to design new SCO compounds is the family of two-dimensional (2D) Hofmann-type coordi-
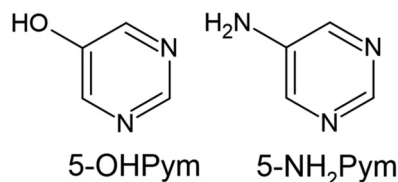
nation polymers (HCPs) formulated as $\{Fe(L)_2[M(CN)_n]_m\}$ (where L is a pyridine, pyrimidine, pyrazole, imidazole or triazole type axial ligand and $M = Pt^{II}$, Pd^{II}, Ni^{II} ($n = 4$; $m = 0$) or Ag^I, Au^I ($n = 2$, $m = 2$)).[23–28] This family of HCPs offers the structural flexibility required to achieve a synergistic interaction of SCO with additional functions by direct replacement of the aromatic ligands in the apical positions of the Fe^{II} sites. A recent example highlighting this strategy involves the functionalization of the axial pyridine with an anthracene fluorescent agent affording the compounds $\{Fe(AnPy)_2[M(CN)_2]_2\}$ (AnPy = 9-anthracenepyridine, M = Au, Ag) which display luminescence coupled to SCO.[29]

Recently, we reported a new family of 2D HCPs formulated as $\{Fe(5-NH_2Pym)_2[M(CN)_4]\}\cdot x$guest ($\mathbf{1(NH_2)^M\cdot x}$**guest**; 5-NH$_2$Pym = 5-aminopyrimidine; M = Pd^{II}, Pt^{II}; guest = H$_2$O, MeOH, EtOH; $x = 0$–1) in which the amino group was introduced for synergistic modulation of SCO with the uptake of guests by single crystal to single crystal transformation.[30] The interplay between SCO and host–guest chemistry in $\mathbf{1}$ $\mathbf{(NH_2)^M\cdot x}$**guest** encouraged us to investigate the influence of pyrimidine functionalization on tailoring the SCO in isostructural $\{Fe(5-OHPym)_2[M(CN)_4]\}\cdot x$guest frameworks ($\mathbf{1}$ $\mathbf{(OH)^M\cdot x}$**guest**, M = Pt, Pd; guest = H$_2$O, MeOH, EtOH; $x = 0$–1), prepared by substitution of 5-NH$_2$Pym with 5-OHPym (5-hydroxypyrimidine) (Scheme 1), which was selected to enhance the host–guest interactions. In fact, the higher ability of the hydroxy moiety to establish H-bonds[32] results in a network of soft supramolecular interactions capable of accommodating structural changes for a richer diversity of SCO responses that include one, two and three step spin transitions in a broad temperature range.

Results

Synthesis and SCO of $\mathbf{1(OH)^M\cdot H_2O}$ (M = Pt, Pd)

Compounds $\mathbf{1(OH)^M\cdot H_2O}$ (M = Pt, Pd) were synthesized as single crystals through liquid phase slow diffusions using methanol–water solutions of the precursors Fe(BF$_4$)$_2$·6H$_2$O, K$_2$[M(CN)$_4$] (M = Pt or Pd) and 5-OHPym (see the Experimental section in the ESI† for more details). Yellow plate-shaped single crystals were obtained after four weeks with yields of about 60–80%. Elemental and thermogravimetric analyses (EA and TGA) of the as-synthesized crystals are consistent with the proposed formula $\{Fe(5-OHPym)_2[M(CN)_4]\}\cdot H_2O$ where the crystallization water molecule is quite labile and can be com-

pletely released by heating above 340 K (see the Experimental section and Fig. S1†). However, it is rapidly recovered when the sample is exposed to air moisture at room temperature (see below).

The SCO properties were studied by recording the thermal dependence of the $\chi_M T$ product (χ_M is the molar magnetic susceptibility and T is the temperature) of pristine crystals of $\mathbf{1}$ $\mathbf{(OH)^M\cdot H_2O}$ (M = Pt, Pd). Fig. 1 shows the resulting $\chi_M T$ $vs.$ T plots together with those of the previously reported analogues $\mathbf{1(NH_2)^M\cdot H_2O}$ (M = Pt, Pd)[28] for comparison. Above 260 K, both $\mathbf{1(OH)^{Pt}\cdot H_2O}$ and $\mathbf{1(OH)^{Pd}\cdot H_2O}$ exhibit a $\chi_M T$ value of $ca.$ 3.5 cm^3 K mol^{-1}, which is in good accord with the Fe^{II} ions being in the HS state. Upon cooling, $\chi_M T$ drops abruptly delineating a two-step profile with $T_{c1}\downarrow/T_{c2}\downarrow = 241.5/219.5$ K for $\mathbf{1}$ $\mathbf{(OH)^{Pt}\cdot H_2O}$ and 254/223.5 K for $\mathbf{1(OH)^{Pd}\cdot H_2O}$ ($T_{ci}\downarrow/T_{ci}\uparrow$ is the temperature at which 50% of the Fe^{II} ions have switched the spin state in each step (i) upon cooling/heating). The two steps
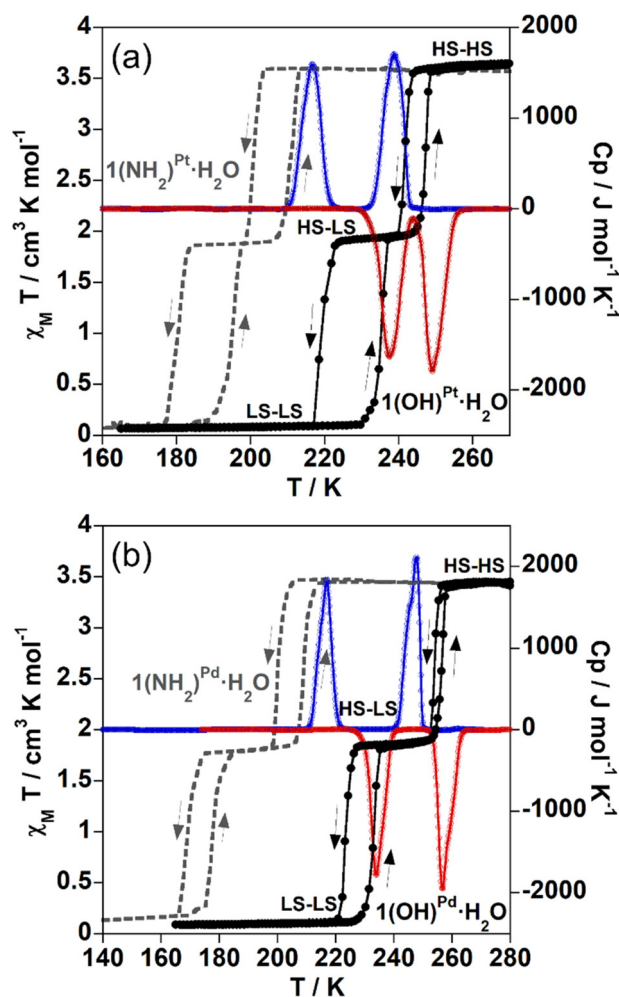

Fig. 1 $\chi_M T$ $vs.$ T (1 K min^{-1} scan rate, black circles) and C_p $vs.$ T (10 K min^{-1} scan rate, blue and red lines for the cooling and heating modes, respectively) plots of (a) $\mathbf{1(OH)^{Pt}\cdot H_2O}$ and (b) $\mathbf{1(OH)^{Pd}\cdot H_2O}$. Magnetic data of the corresponding $\mathbf{1(NH_2)^M\cdot H_2O}$ analogues (grey dashed lines) have also been included for comparison. Grey and black arrows indicate the direction of the cooling and heating modes.

Scheme 1 Structure of ligands 5-hydroxypyrimidine (5-OHPym) and 5-aminopyrimidine (5-NH$_2$Pym).

This journal is © the Partner Organisations 2023

Inorg. Chem. Front., 2023, **10**, 600–611 | **601**

are separated by an intermediate plateau at $\chi_M T \approx 1.8$ cm^3 K mol^{-1} corresponding to a 50% mixed HS–LS state. This intermediate state is stable in the temperature ranges of 240–220 K (Pt) and 250–230 K (Pd). Below *ca.* 215 K, the $\chi_M T$ value of both derivatives is about 0.06 cm^3 K mol^{-1} which is consistent with all Fe^{II} ions exhibiting a diamagnetic LS state and, therefore, revealing a complete spin transition. This double step behaviour is reproduced upon heating although the curves are shifted to higher temperatures for both derivatives, thereby defining hysteresis loops ($\Delta T_i = T_{ci}\uparrow - T_{ci}\downarrow$) $\Delta T_1/\Delta T_2 = 6/15$ K (**1(OH)^{Pt}·H$_2$O**) and 2/8 K (**1(OH)^{Pd}·H$_2$O**). As observed in Fig. 1, even if the two-stepped shape of the magnetic curves is maintained, the substitution of NH$_2$ with OH in the axial pyrimidine ring provokes a remarkable increase of the SCO temperatures of about 40–60 K.

The SCO properties of **1(OH)^M·H$_2$O** (M = Pt, Pd) were also investigated by differential scanning calorimetry (DSC) which was carried out with a scan rate of 10 K min^{-1}. The anomalous variation of the molar specific heat (C_p) *vs.* T is presented in Fig. 1 together with the magnetic behaviour for comparison. The C_p *vs.* T plots of both Pt and Pd derivatives show two maxima ($T_{c1}\downarrow = 238.7$ K and $T_{c2}\downarrow = 216.7$ K for Pt and $T_{c1}\downarrow = 247.8$ K and $T_{c2}\downarrow = 216.9$ K for Pd) and two minima ($T_{c1}\uparrow = 249.1$ K and $T_{c2}\uparrow = 237.7$ K for Pt and $T_{c1}\uparrow = 256.7$ K and $T_{c2}\uparrow = 233.9$ K for Pd) in the cooling and heating modes, respectively. The average values of the total variation of entropy (ΔS) and enthalpy (ΔH) are 84.84 J K^{-1} mol^{-1} and 20.48 kJ mol^{-1} for **1(OH)^{Pt}·H$_2$O** and 82.08 J K^{-1} mol^{-1} and 19.54 kJ mol^{-1} for **1(OH)^{Pd}·H$_2$O**. These results are consistent with a complete two-step SCO, in good agreement with the magnetic measurements. The differences in the SCO temperatures are attributed to the different scan rates used for each technique (1 K min^{-1} *vs.* 10 K min^{-1}).

Structure of 1(OH)^M·H$_2$O (M = Pt, Pd)

The crystal structures of **1(OH)^M·H$_2$O** (M = Pt, Pd) were successfully resolved through single crystal X-ray diffraction (SCXRD) and analysed at different significant temperatures in the 120–270 K range. Crystallographic data and a selection of relevant bond lengths and angles are gathered in Tables S1–S4.†

Compounds **1(OH)^M·H$_2$O** (M = Pt, Pd), which are isomorphous to the analogous **1(NH$_2$)^M·H$_2$O** system, crystallize in the monoclinic *C2/m* space group. The asymmetric unit contains two distinct octahedral Fe^{II} centrosymmetric sites which are hereafter labelled as Fe1 and Fe2 (Fig. 2a). The equatorial positions are coordinated by the N atoms (Fe1–N3 and Fe2–N4) of four equivalent bridging tetracyanometallate units whereas the axial positions are coordinated by one of the two heterocyclic N atoms (Fe1–N1 and Fe2–N5) of two equivalent terminal 5-OHPym ligands. The bridging coordination mode of the tetracyanometallate anions and the monotopic coordination mode of the 5-OHPym ligands result in the formation of extended 2D bimetallic layers (Fig. 2b) that stack to form a 3D supramolecular packing (Fig. 2c). This packing is stabilized through weak π···π interactions operating between the interdi-
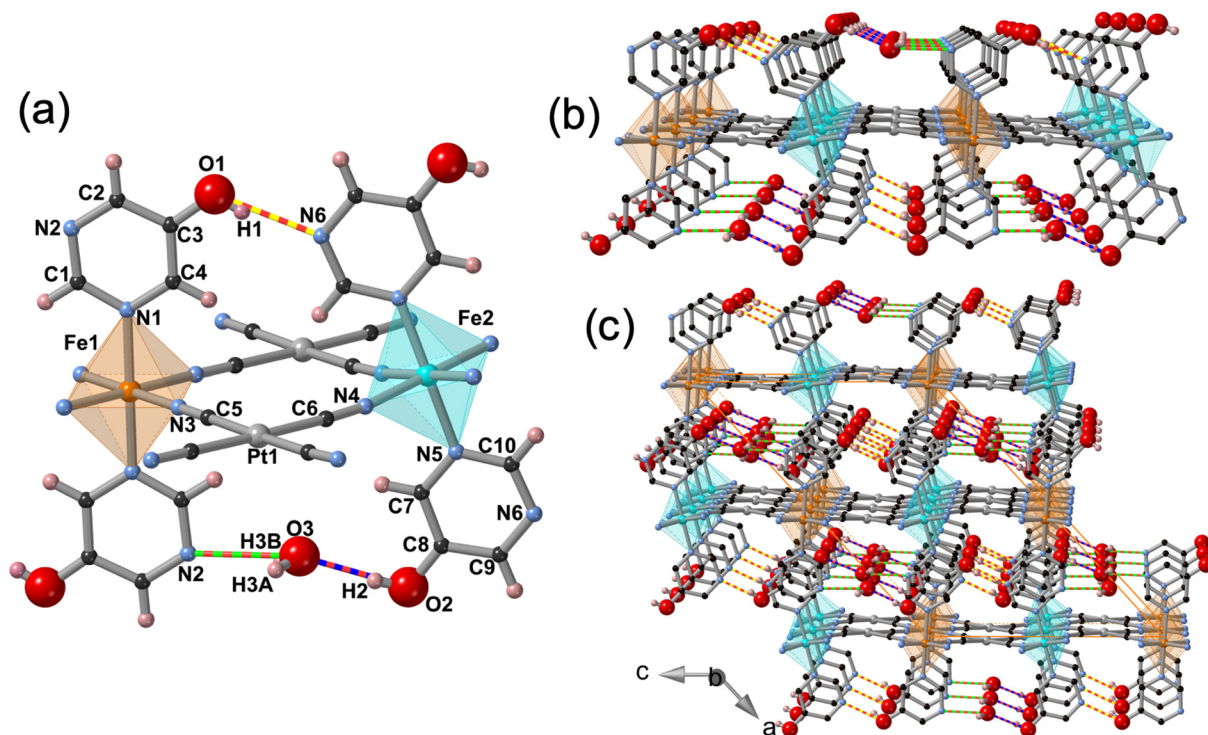

Fig. 2 (a) Molecular fragment of **1(OH)^{Pt}·H$_2$O** (isomorphous to **1(OH)^{Pd}·H$_2$O**) showing the atom numbering of the asymmetric unit. (b) View of a single bimetallic layer. (c) Packing of three consecutive bimetallic layers displaying the water guest molecules adsorbed along the channels. The inter- and intramolecular H-bonds are highlighted with green-red (N2···O3)/blue-red (O3···O2) and yellow-red (O1···N6) dashed lines, respectively.

602 | *Inorg. Chem. Front.*, 2023, **10**, 600–611

This journal is © the Partner Organisations 2023

gitated 5-OHPym ligands of adjacent layers (Fig. S2†) and by the formation of an intricate network of H-bonds. Some of these H-bonds are promoted by one molecule of water located in two discrete equivalent positions along the 1D channels generated between the stacked layers (Fig. 2c and Fig. S3†). Within a given layer, this molecule of water interacts simultaneously with the free nitrogen of the 5-OHPym ligand coordinated to Fe1 (N2···O3) and with the hydroxy group of the contiguous 5-OHPym ligand coordinated to Fe2 (O3···O2) (Fig. 2a and b). Additionally, each water molecule interacts with its neighbouring ones located within the same channel (O3···O3) (see Fig. S3† and Table 1). Furthermore, the relative orientation of the 5-OHPym axial ligands enables an intralayer H-bond (O1···N6) established between the hydroxy group of the 5-OHPym ligand coordinated to Fe1 and the non-coordinated nitrogen of the adjacent 5-OHPym ligand coordinated to Fe2. The latter interaction is responsible for the slight undulation observed for the bimetallic layers which arises from the angle defined by the equatorial planes Fe1 $(N3)_4$/Fe2$(N4)_4$ with that of $[M(CN)_4]$ of 3.42/19.67° (Pt) and 6.74/22.11° (Pd) at 260 K.

Although the overall structure described above is maintained upon changing the temperature (the space group remains unaltered), important thermally induced variations have been observed in the iron to nitrogen average bond length $\langle$Fe–N$\rangle$ of the Fe1 and Fe2 sites. At 270–260 K, the $\langle$Fe1–N$\rangle$/$\langle$Fe2–N$\rangle$ values for $1(OH)^{Pt}\cdot H_2O$ ($1(OH)^{Pd}\cdot H_2O$) equal to 2.166/2.148 Å (2.179/2.165 Å) are perfectly consistent with the HS state. Then, they change to 2.161/1.964 Å (2.163/1.955 Å) and 1.964/1.960 Å (1.965/1.953 Å) upon successively cooling

down to 240–230 K, and 200 K, respectively. Considering that a complete HS-to-LS transition involves a decrease in $\langle$Fe–N$\rangle$ of *ca.* 0.20 Å, these observations indicate a complete SCO defining the sequence Fe1(HS)–Fe2(HS) ↔ Fe1(HS)–Fe2(LS) ↔ Fe1 (LS)–Fe2(LS) which is consistent with the two-step SCO observed through the magnetic measurements (Fig. 1 and Table 2).

SCO of $1(OH)^M$ (M = Pt, Pd)

As mentioned above, the water guest molecule can be easily removed from $1(OH)^M\cdot H_2O$ to yield the dehydrated $1(OH)^M$ counterparts. The release of water involves notable modifications of the SCO properties moving from a double to a single step transition with $T_c\downarrow/T_c\uparrow$ equal to 204/224 K (Pt) and 214/232 K (Pd) featuring 20 and 18 K wide hysteresis loops, respectively (Fig. 3). In contrast with the considerable increase in T_c (40–60 K) observed when moving from $1(NH_2)^M\cdot H_2O$ to $1(OH)^M\cdot H_2O$, solvent free $1(NH_2)^{Pt}$ and $1(OH)^{Pt}$ compounds show similar SCO temperatures with a difference in average T_c of only 4 K while a moderate increase of 25 K is observed when moving from $1(NH_2)^{Pd}$ to $1(OH)^{Pd}$ (Fig. S4†). Besides, in both derivatives the hysteresis width is larger for the hydroxy functionalized derivatives.

The SCO properties of $1(OH)^M$ (M = Pd, Pt) were also analyzed through calorimetric measurements which showed a unique anomaly for both the cooling [$T_c\downarrow$ = 184 (Pt) and 202 K (Pd)] and the heating [$T_c\uparrow$ = 220 (Pt) and 228 K (Pd)] modes with average ΔS (J mol^{-1} K^{-1})/ΔH (kJ mol^{-1}) values of 64.62/13.01 (Pt) and 74.79/16.03 (Pd). These results indicate a complete one step spin transition, in good agreement with the $\chi_M T$

Table 1 Selected H-bond distances (in Å) found for $1(OH)^M$, $1(OH)^M\cdot H_2O$ and $1(OH)^M\cdot MeOH$ (M = Pt, Pd) at 260 K

	Interaction	$1(OH)^{Pt}$	$1(OH)^{Pd}$	$1(OH)^{Pt}\cdot H_2O$	$1(OH)^{Pd}\cdot H_2O$	$1(OH)^{Pt}\cdot MeOH$	$1(OH)^{Pd}\cdot MeOH$	$1(OH)^{Pt}\cdot EtOH$
Host–host	O1(hydroxy)···N6(het.)	2.745	2.774	2.785	2.793	2.735	2.780	2.886
Host–guest	O3(guest)···N2(het.)	—	—	2.906	2.941	2.904	2.857	2.588
	O3(guest)···O2(hydroxy)	—	—	2.849	2.814	2.865	2.774	3.078
Guest–guest	O3(guest)···O3(guest)	—	—	2.592	2.568	—	—	—

Table 2 Octahedral distortion parameters (Θ and Σ)[31] at different temperatures and the associated Fe–N average distances for $1(OH)^M\cdot H_2O$ and $1(OH)^M$ (M = Pt, Pd)

Sample	$1(OH)^{Pt}\cdot H_2O$						$1(OH)^{Pt}$	
T (K)	260		230		120		260	120
Spin state	Fe1(HS)	Fe2(HS)	Fe1(HS)	Fe2(LS)	Fe1(LS)	Fe2(LS)	HS	LS
Fe–N (Å)	2.166	2.148	2.161	1.964	1.964	1.953	2.163	1.951
Θ/Σ	34/14	28/8	33/21	21/13	21/7.5	23/11	33.7/15.1	22.0/7.5

Sample	$1(OH)^{Pd}\cdot H_2O$						$1(OH)^{Pd}$	
T (K)	270		240		180		260	180
Spin state	Fe1(HS)	Fe2(HS)	Fe1(HS)	Fe2(LS)	Fe1(LS)	Fe2(LS)	HS	LS
Fe–N (Å)	2.179	2.165	2.165	1.955	1.956	1.955	2.159	1.957
Θ/Σ	35/18	26/9	46/28	17/12	27/13	18/9	40.1/17.7	23.4/12.2

This journal is © the Partner Organisations 2023

Inorg. Chem. Front., 2023, **10**, 600–611 | **603**
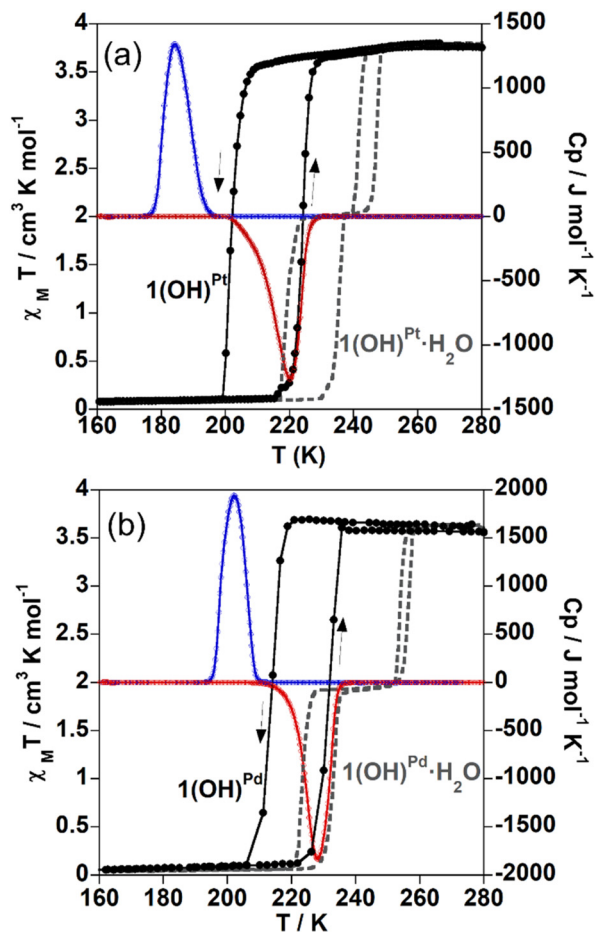
Fig. 3 $\chi_M T$ vs. T (1 K min^{-1} scan rate, black circles) and C_p vs. T (10 K min^{-1} scan rate, blue and red lines for the cooling and heating modes, respectively) plots of (a) **1(OH)^{Pt}** and (b) **1(OH)^{Pd}**. Magnetic data of the corresponding **1(OH)^{M}·H$_2$O** derivatives (grey dashed lines) have also been included for comparison.

vs. T measurements (Fig. 3). The discrepancies in the SCO temperatures between the magnetic and calorimetric measurements can be ascribed to the different scanning rates used for each technique.

Structural study of the 1(OH)^{M}·H$_2$O → 1(OH)^{M} dehydration

Since the dehydration process takes place in a single crystal to single crystal manner, SCXRD was used to delve into the structural changes accompanying the loss of water. Thus, a single crystal of **1(OH)^{M}·H$_2$O** was heated at 400 K on a diffractometer, then cooled back to 260 K and measured to determine its structure. Crystallographic data and a selection of relevant bond lengths and angles are gathered in Tables S1–S4.† The resulting orthorhombic *Pnma* asymmetric unit is formed by a unique pseudo-octahedral Fe^{II} site with four equivalent [M(CN)$_4$]$^{2-}$ anions coordinating the equatorial positions and two distinct monotopic 5-OHPym ligands occupying the apical coordination sites (Fig. 4a). Even if, similarly to **1(OH)^{M}·H$_2$O**, the Fe^{II} ions are connected through the [M(CN)$_4$]$^{2-}$ anions

defining bimetallic layers (Fig. 4b) which stack to form a 3D packing (Fig. 4c), the lack of water within the structure confirms that the dehydration occurs upon heating. Indeed, the water release takes place along with an important structural change involving 180° rotation of half of the 5-OHPym ligands, the ones involved in the H-bonds with the guest water molecule. As a result, they change from the transoid conformation observed for the hydrated structures (Fig. 2a and b) to the cisoid conformation observed for the dehydrated ones (Fig. 4a and b). In addition, because of the absence of water, the H-bonds are now limited to the N6(hetero)···O1(hydroxy) intralayer interactions which, in turn, are slightly strengthened with respect to **1(OH)^{M}·H$_2$O** (Table 1). This is probably the reason why the rearrangement of the structure after water desorption involves a notable increase of the layer undulation (see Fig. 2b and 4b). Indeed, the two different angles formed between the equatorial planes defined by [FeN(3/4)$_4$] and [M(CN)$_4$] are 6.47/24.38° (Pt) and 12.03/28.72° (Pd) at 260 K.

The **1(OH)^{M}·H$_2$O → 1(OH)^{M}** (M = Pt, Pd) process was also monitored *in situ* through powder X-ray diffraction (PXRD) in a temperature and atmosphere-controlled chamber (see the Experimental section in the ESI†). In the case of the Pt derivatives, a PXRD pattern was first recorded for a pristine compound of **1(OH)^{Pt}·H$_2$O** at 303 K. The comparison of the resulting pattern with that simulated from SCXRD confirmed that the starting sample is the monohydrated compound (Fig. S5†). Then, the sample was heated under a dry N$_2$ atmosphere and successive patterns were collected every 10 K under stable temperatures. After an intermediate state at 323 K, the dehydration process was subsequently completed at 333 K. These pattern changes were straightforwardly monitored using as a marker the intense [200] peak at 2θ = 10.9°, characteristic of **1(OH)^{Pt}·H$_2$O**, which vanishes to give rise to a new peak at around 11.1°. Compared with the corresponding simulated pattern, the latter, indexed to [002], can be associated with **1(OH)^{Pt}** confirming that the dehydration takes place effectively. Furthermore, the main 2θ up-shift of the remaining peaks indicates a general contraction of the packing consistent with the release of water. In the case of the Pd counterpart, similar changes in the PXRD patterns were observed, even though in this case, the water molecule was more labile and was gradually released at 298 K under a dry N$_2$ stream without further heating (Fig. S6†).

Guest adsorption studies

The PXRD, TGA and isothermal adsorption results have revealed that the solvent free compounds **1(OH)^{M}** (M = Pt, Pd) are prone to re-adsorb small protic molecules such as water, methanol or ethanol yielding **1(OH)^{M}·H$_2$O**, **1(OH)^{M}·xMeOH** (x = 0–1) or **1(OH)^{M}·xEtOH** (x = 0–0.8).

The re-adsorption processes were monitored through *in situ* PXRD measurements. Although the described results will be based on the Pt derivative (Fig. 5), a similar behaviour was observed for the Pd one (Fig. S7†). First, a pristine sample of **1(OH)^{Pt}·H$_2$O** was dehydrated *in situ* in the diffractometer chamber under a constant N$_2$ flow. Next, the N$_2$ current was
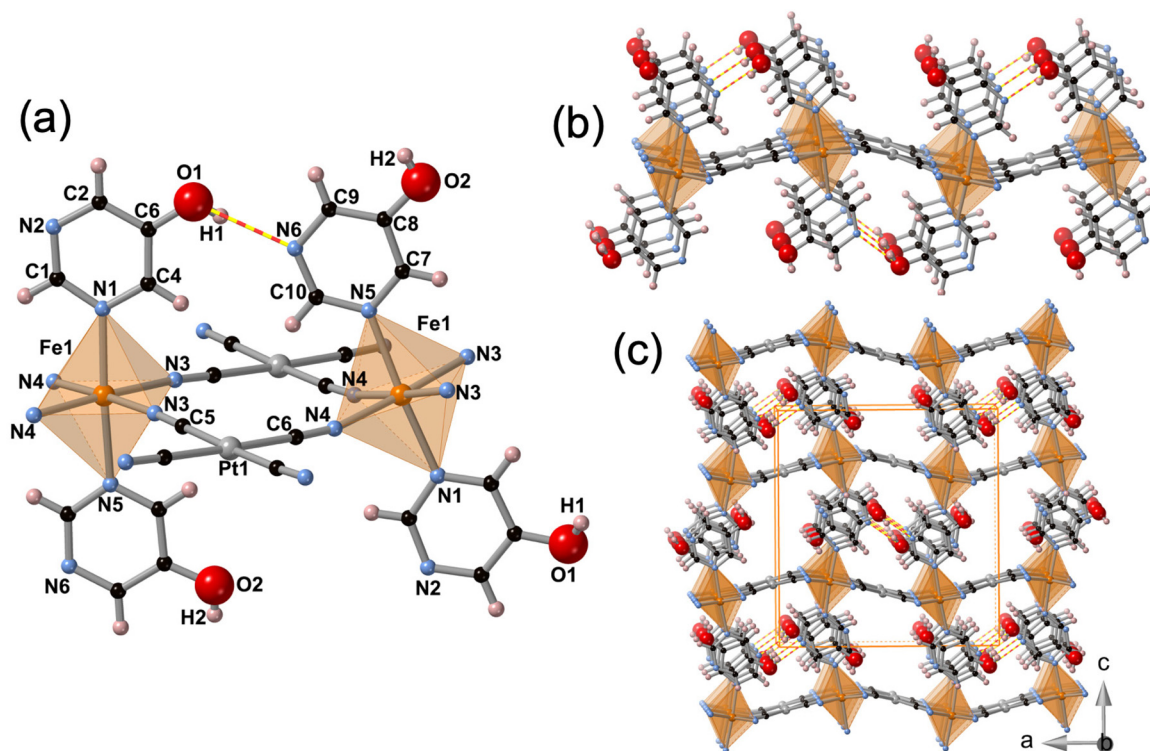
604 | *Inorg. Chem. Front.*, 2023, **10**, 600–611

This journal is © the Partner Organisations 2023

Fig. 4 (a) Molecular fragment of **1(OH)^{Pt}** (isomorphous to **1(OH)^{Pd}**) showing the atom numbering of the asymmetric unit, (b) view of a single bi-metallic layer and (c) packing of four consecutive bimetallic layers. The intramolecular H-bonds are highlighted with red-yellow (O1···N6) dashed lines.
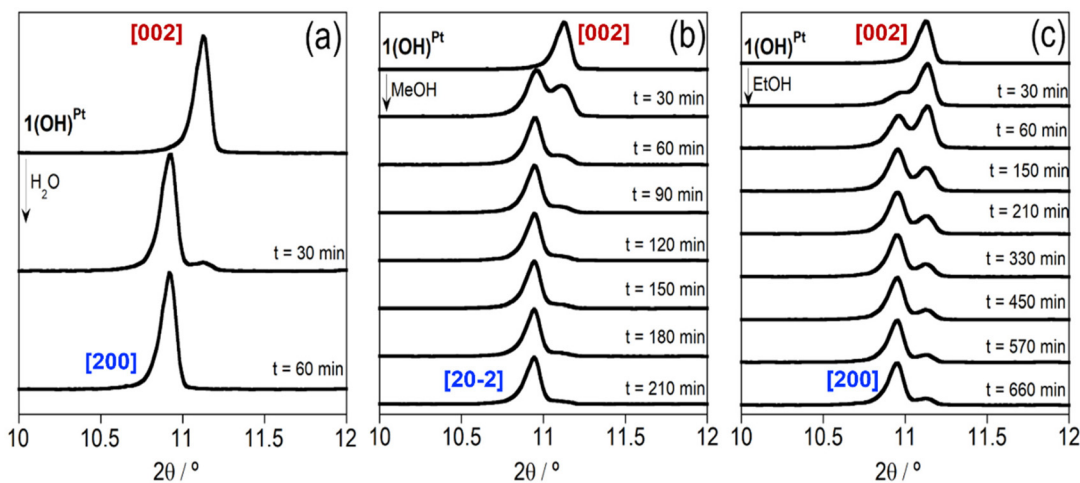

Fig. 5 Evolution with time of the PXRD patterns of compound **1(OH)^{Pt}** upon exposure to a N_2 flow saturated with (a) water, (b) methanol and (c) ethanol at room temperature.

saturated with a guest solvent (guest = water, methanol or ethanol) at room temperature and successive PXRD patterns were acquired every *ca.* 30 minutes. The structural modifications induced by the guest uptake were examined by focusing on the variations noted in the intense [002] peak at 11.10°, characteristic of the guest-free **1(OH)^{Pt}** compound. Regardless

of the used guest, the adsorption provokes a decrease in the intensity of this peak and an increase of a new peak at 10.95–10.99°, which corresponds to the [200] (or [20−2]) diffraction line of the solvated counterpart (Fig. 5). However, the rapidity at which the intensity ratio between the two peaks changes clearly depends on the guest nature and shows their

different diffusivities into the 2D HCP. Hence, whereas the adsorption of water from air moisture is practically completed within the first 30 minutes (Fig. 5a), those of methanol and ethanol show slower diffusions (Fig. 5b and c). In the case of methanol, even though the adsorption process seems to be almost complete after 60 minutes, it takes two additional hours for the dehydrated [002] peak to disappear entirely. The ethanol adsorption process is very gradual and remains incomplete even after 12 hours. The reversibility of the adsorption process was also investigated by examining the changes in the diffractograms when re-heating the **1(OH)^{Pt}·guest** samples. In all cases, the adsorption is fully reversible and the diffractogram of the activated **1(OH)^M** compound is recovered after heating (or even without heating for the Pd derivatives) the samples above 333 K under a dry N_2 stream (Fig. S8 and S9†).

The adsorption processes were also analysed through TGA measurements. To this end, the hydrated forms **1(OH)^{Pt}·H$_2$O** and **1(OH)^{Pd}·H$_2$O** were first dehydrated inside the TGA chamber to obtain the desolvated **1(OH)^M** counterparts. Then, a N_2 flow saturated with the guest (guest = water, methanol or ethanol) was continuously passed through the sample and the gain of mass was recorded at room temperature. As observed in Fig. 6, methanol produces an abrupt increase of mass within the first 10–12 minutes for both **1(OH)^{Pt}** and **1(OH)^{Pd}**, followed by a gradual stabilization of the curve. This is consistent with a rapid adsorption of 0.3–0.4 molecules of methanol followed by a gradual uptake of up to *ca.* 0.5 molecules after 80 minutes. In contrast, both **1(OH)^{Pt}** and **1(OH)^{Pd}** exhibit a

certain resistance to the adsorption of water within the first 5 (Pt) and 12 (Pd) minutes which is subsequently overcome to describe a sigmoidal curve that saturates at 0.8–0.9 molecules of water after 80 minutes. Finally, the adsorption of ethanol is very gradual and reaches very low adsorption rates. This is especially true for **1(OH)^{Pd}** which, under these conditions, barely adsorbs 0.07 molecules of ethanol after 11 hours while **1(OH)^{Pt}** adsorbs *ca.* 0.4 within the same period of time. Comparatively, the Pt derivatives adsorb faster and show higher amounts of adsorbed guest than the Pd derivatives (see Fig. S10†). Besides, the hydroxy-functionalized networks **1 (OH)^M** exhibit more cooperative adsorptions than the previously reported **1(NH$_2$)^M** ones and achieve higher amounts of adsorbed guest (Fig. S11†).

Additionally, water, methanol and ethanol adsorption isotherms were recorded for the previously activated **1(OH)^{Pt}** and **1(OH)^{Pd}** compounds (Fig. 7). Note that the reported isotherms of compounds **1(NH$_2$)^{Pt}** and **1(NH$_2$)^{Pd}**[30] are also depicted for comparison. Analogously to that observed for **1(NH$_2$)^M**, the **1 (OH)^M** host frameworks seem to exhibit higher affinity (*i.e.* higher amounts of adsorbed analyte at lower pressures) for alcohols than for water. This is clearly reflected in the isotherms of **1(OH)^{Pd}** (Fig. 7d) where, while methanol begins to adsorb at a relative guest pressure (P/P_0) below 0.01, water only starts above $P/P_0 = 0.06$. The latter behaviour reveals a gate opening effect for water adsorption, similar to that observed for the **1(NH$_2$)^{Pd}** compounds, but at lower pressures. However, no gate opening is observed for **1(OH)^{Pt}** for which all guests start adsorbing from very low guest pressures (Fig. 7b). Although the adsorption of water in **1(OH)^{Pd}** occurs above a

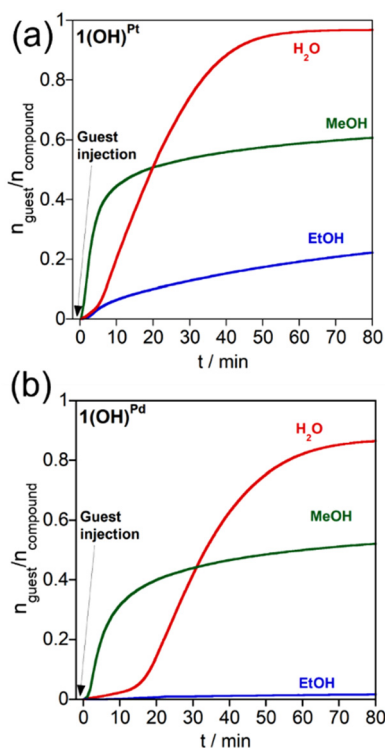**Fig. 6** Time dependent TGA showing the uptake of H_2O, MeOH and EtOH by (a) **1(OH)^{Pt}** and (b) **1(OH)^{Pd}**.
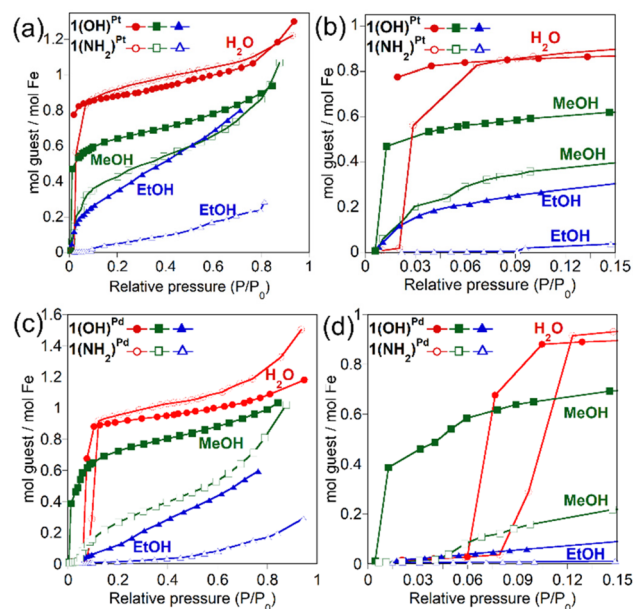
Fig. 7 (a and c) Water, methanol and ethanol adsorption isotherms (full points) of **1(OH)^{Pt}** and **1(OH)^{Pd}** and (b and d) the corresponding enlarged plots in low pressure ranges. The adsorption isotherms of **1(NH$_2$)^M** (M = Pt, Pd) analogues (open points) are also displayed for comparison.

606 | *Inorg. Chem. Front.*, 2023, **10**, 600–611

This journal is © the Partner Organisations 2023

certain threshold value, it takes place in an abrupt and concerted manner with the adsorption of *ca.* 0.8 molecules of water per mol of compound within a narrow interval of pressures, saturating to one molecule of water at higher pressures ($P/P_0 = 0.6$–0.8). In the case of methanol adsorption, $1(OH)^M$ adsorbs rapidly 0.5 molecules at very low pressures and gradually reaches *ca.* one molecule at $P/P_0 = 0.8$. In contrast, ethanol is adsorbed very gradually, only reaching 0.6–0.8 adsorbed molecules at high pressures.

SCO of $1(OH)^M \cdot x$MeOH ($x = 0$–1) and $1(OH)^M \cdot x$EtOH ($x = 0$–0.8)

The influence of the adsorption of methanol/ethanol on the SCO properties of $1(OH)^M$ (M = Pd, Pt) was investigated through the study of the $\chi_M T$ variation as a function of temperature. Aiming at assessing the evolution of the SCO with increasing amounts of adsorbed guest, the $\chi_M T$ *vs. T* curves were recorded for the previously dehydrated $1(OH)^M$ compounds immediately immersed in pure methanol or ethanol baths for 15 minutes, 14 hours (overnight) and 3 days. According to the TGA, the quantity of adsorbed guest after 3 days is one molecule of methanol (both for Pt and Pd) and 0.8/0.5 molecules of ethanol (for Pt/Pd) per Fe^{II} ion (Fig. S12†).

The adsorption of methanol induces a three-step SCO which is observable after 15 minutes of immersion for both the Pt and Pd derivatives (Fig. 8a and b). Indeed, the longer they stay in contact with methanol, the more marked are the steps, the lower are the SCO temperatures, and the higher are the HS residual fractions (*i.e.* the higher the $\chi_M T$ values at low

Fig. 8 Evolution of the $\chi_M T$ *vs. T* plots of $1(OH)^{Pt}$ and $1(OH)^{Pd}$ after being immersed in (a and b) pure methanol or (c and d) ethanol baths for 15 minutes (black curves), overnight (blue curves) and for three days (red curves). The SCO of the unsolvated compounds is depicted with grey curves.

temperatures). Moreover, hysteresis loops, which gradually widen with immersion time, are observed for the three steps.

In the case of ethanol adsorption, the $\chi_M T$ *vs. T* curves observed for both derivatives after 15 minutes of immersion display a two-step SCO which appears to be the result of a mixture of the desolvated and the solvated forms. Indeed, at higher immersion times, this two-step behaviour evolves into a more gradual and incomplete transition at lower temperatures. Moreover, in contrast to that observed for methanol adsorption, the hysteresis loop narrows gradually with immersion time. This effect is more marked for the Pt derivative for which a gradual spin conversion with a narrow hysteresis (<5 K) is observed after 3 days.

Structures of $1(OH)^M \cdot 0.5$MeOH (M = Pt, Pd) and $1(OH)^{Pt} \cdot 0.5$EtOH

The structures of $1(OH)^M \cdot 0.5$MeOH (M = Pt, Pd) and $1(OH)^{Pt} \cdot 0.5$EtOH were determined from the crystals obtained by dehydrating selected crystals of $1(OH)^M \cdot H_2O$ in the diffractometer chamber and immersing the activated compounds in the corresponding solvent overnight (three days in the case of EtOH). Crystallographic data and a selection of relevant bond lengths and angles are displayed in Tables S5–S10.† The structural resolution of $1(OH)^{Pd} \cdot EtOH$ was not achieved probably due to the simultaneous presence of solvated and desolvated forms within the same crystal. The structures of $1(OH)^M \cdot MeOH$ (M = Pt, Pd) could not be obtained since the crystals lost their crystallinity after 3 days of immersion in pure methanol. Crystals of $1(OH)^M \cdot 0.5$MeOH (M = Pt, Pd) and $1(OH)^{Pt} \cdot 0.5$EtOH display the monoclinic $C2/m$ space group with an asymmetric unit analogous to that of $1(OH)^M \cdot H_2O$. Half a molecule of methanol (or ethanol) per unit formula is clearly localized in the pores and interacts, similarly to water, with the host 5-OHPym ligands (Fig. 9a and Fig. S13†). Nevertheless, the specific position of the oxygen atom within the pores is not equivalent for MeOH/EtOH and H_2O. This is a consequence of the accommodation of the aliphatic moiety of the former within the channels while optimizing the host–guest interactions (Table 1). Analogously to $1(OH)^M \cdot H_2O$, the two different Fe^{II} ions (Fe1 and Fe2) are connected through the $[M(CN)_4]^{2-}$ ions to produce undulated bimetallic layers which stack creating channels where the methanol/ethanol molecules are located.

Considering the three-step SCO observed for $1(OH)^M$ (M = Pt, Pd) after being immersed in MeOH overnight (Fig. 8a and b), the structures of $1(OH)^M \cdot 0.5$MeOH were studied at 260, 215 (Pt)/225 (Pd), 160 (Pt)/195 (Pd) and 120 K. Although the same space group is maintained upon cooling, a stepped decrease of the $\langle Fe1–N \rangle / \langle Fe2–N \rangle$ average distances (see Table 3) was detected within this range of temperature indicating a progressive HS-to-LS transformation in the crystal. In order to monitor the spin state change, the unit cell volume at each temperature is presented together with the magnetic behaviour for comparison (Fig. 9b and c). Indeed, the thermal evolution of the unit cell volume is in excellent accord with that
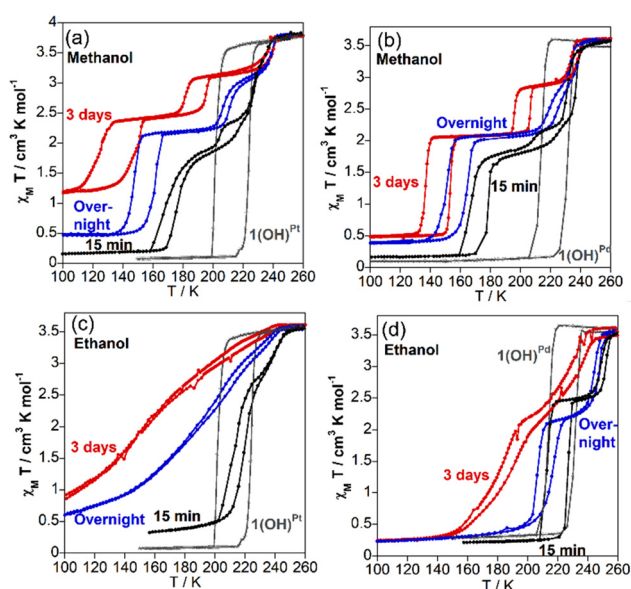
Table 3 Average Fe–N bond lengths (in Å) of Fe1 and Fe2 sites at different temperatures for **1(OH)^M·0.5MeOH** (M = Pt, Pd)

T (K)	**1(OH)^{Pt}·0.5MeOH**		**1(OH)^{Pd}·0.5MeOH**	
	(Fe1–N)$_{av}$	(Fe2–N)$_{av}$	(Fe1–N)$_{av}$	(Fe2–N)$_{av}$
260	2.175	2.159	2.166	2.146
215/225	2.131	2.087	2.123	2.067
160/195	2.122	1.972	2.075	2.019
120	1.965	1.963	1.958	1.957

0.2 Å), thereby suggesting an incomplete spin transition (*ca.* 13% of Fe^{II} remains in the HS state) as determined from the magnetic measurements.

Discussion

Motivated by our recent study on the 2D HCPs **1(NH$_2$)^M·xguest** (M = Pt, Pd; x = 0–1; guest = H$_2$O, MeOH, EtOH) bearing 5-NH$_2$Pym as the axial ligand, we performed the synthesis, structural study and SCO characterization of the homologous hydroxy-functionalized materials **1(OH)^M·xguest** (M = Pt, Pd; x = 0–1; guest = H$_2$O, MeOH, EtOH). Although both systems are equivalent from a structural point of view, the replacement of –NH$_2$ with –OH markedly influences not only the ability of the material to adsorb protic guests but also the extent to which these guests affect the SCO properties.

In the desolvated counterparts **1(NH$_2$)^M** and **1(OH)^M**, the bimetallic layers show marked corrugation as a solution to maximize the H-bond interaction established between the complementary pairs of adjacent 5-XPym ligands within the same layer [(5-XPymFe)H···N(5-XPymFe′), X = NH$_2$, OH]. Furthermore, the corrugation accommodates with minimal steric hindrance the remaining non-H-bonded NH$_2$/OH groups which are further apart defining guest-accessible 1D channels. In this situation, there is only one type of Fe^{II} which undergoes a complete one step SCO. Given the isostructurality of **1(NH$_2$)^M** and **1(OH)^M**, their small differences in SCO temperature (especially when M = Pt^{II} [**1(NH$_2$)^{Pt}**, T_c = 218 K and ΔT_c = 10 K; **1(OH)^{Pt}**, T_c = 214 K and ΔT_c = 20 K]) (see Fig. S4†) may only be associated with a combination of two factors: (i) electronic effects resulting from the inductive/resonant character derived from the substituent and (ii) subtle structural variations around the Fe^{II} centers stemming from different degrees of corrugation (**1(OH)^M** is slightly more corrugated than **1(NH$_2$)^M**) modulated by the H-bond interactions (Fig. S14†). Besides, the stronger H-bonds established by the hydroxy group might be the cause of the larger cooperativity observed for the **1(OH)^M** derivatives (the width of the hysteresis is practically doubled).

Upon exposure to humid air, both **1(OH)^M** and **1(NH$_2$)^M** tend to host water molecules. These guests are accommodated within the accessible space created between contiguous 5-XPym ligands which show a simultaneous 180° rotation. Indeed, this ligand rotation together with a decrease of the
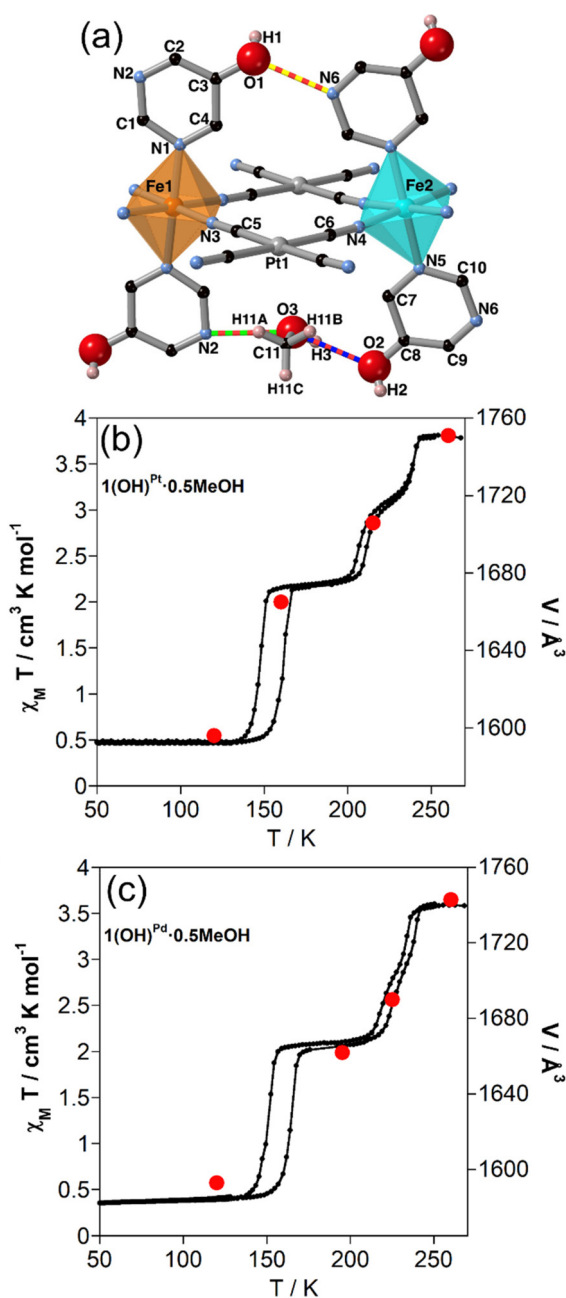
Fig. 9 (a) Fragment of the structure of **1(OH)^M·0.5MeOH** showing the atom labels of the asymmetric unit cell. Thermal evolution of the unit cell volume (red points) for (b) **1(OH)^{Pt}·0.5MeOH** and (c) **1(OH)^{Pd}·0.5MeOH** compared with the magnetic data of crystals immersed in MeOH overnight.

expected from the three-step SCO monitored through the magnetic measurements.

The structure of **1(OH)^{Pt}·0.5EtOH** was resolved at 260 K and 120 K. As expected, a decrease of ⟨Fe1–N⟩ and ⟨Fe2–N⟩ was observed upon cooling, being 2.165 and 2.162 Å at 260 K and 1.997 and 1.982 Å at 120 K. However, the total shortening of ⟨Fe1–N⟩ and ⟨Fe2–N⟩ (0.168 and 0.180 Å, respectively) upon cooling is clearly below that expected for a complete SCO (*ca.*

layer corrugation favours the stabilization of the water guest through a double host–guest H-bonding interaction while simultaneously minimizing the steric repulsions within the network. As a result of this structural rearrangement, the 2D network adopts a more thermodynamically stable conformation which rapidly evolves under ambient conditions. Another consequence of the water adsorption is the generation of two crystallographically distinct Fe^{II} centers (Fe1 and Fe2) which are characterized by having different angular distortions (Θ and Σ) and average bond lengths $\langle Fe-N \rangle$ and therefore different spin transition temperatures. In fact, in the case of **1(NH₂)ᴹ**, the lower angular distortion and $\langle Fe-N \rangle$ values make the LS state more stable for Fe1 which exhibits SCO at higher temperatures than Fe2. Clearly, the inclusion of the water molecule induces elastic frustration between opposite elastic interactions in the network, giving rise to a HS–LS plateau. A remarkable fact is that in spite of being isomorphous, the composition of the mixed spin state is unexpectedly different in each derivative, *i.e.* Fe1(LS)/Fe2(HS) for **1(NH₂)ᴹ** and Fe1(HS)/Fe2(LS) for **1(OH)ᴹ**. This observation may be explained by subtle local structural changes around the Fe^{II} ion induced by the shorter H-bonds established by the hydroxy group which indicates an inversion of the magnitude of the octahedral distortion parameters (Θ and Σ) for Fe1 and Fe2 with respect to **1(NH₂)ᴹ·H₂O** (Fig. S15†). In addition to the cited structural effects, the different H-bonding intensities established between the host structure and the water molecule could modulate the ligand field strength *via* electronic factors contributing to the systematic SCO temperature increase (40–60 K) when moving from the **1(NH₂)ᴹ·H₂O** to the **1(OH)ᴹ·H₂O** frameworks.

When introducing bulkier hydroxylic solvents with an increasing number of C atoms such as MeOH and EtOH, the steric factors become more important, thereby affecting the magneto-structural properties. For example, the inclusion of 0.5 MeOH molecules leads to an important number of short contacts smaller than the sum of the corresponding radii of vdW C(Pym)–O(MeOH) and N/C(Pym)–C(MeOH) (Fig. S16†). As a consequence of the increasing steric hindrance, in the case of **1(NH₂)ᴹ·0.5MeOH**, the SCO of the Fe2 center is shifted to lower temperature with respect to the hydrated derivative, whereas Fe1 remains blocked in the HS state at any temperature. A SCO shift to lower temperatures is also observed in the homologous **1(OH)ᴹ·0.5MeOH** derivatives. However, in this case, the structure appears to be flexible enough to accommodate the additional intermolecular interactions introduced by the MeOH, thus allowing a full HS-to-LS conversion (Fig. S17†). Indeed, at 260 K, the shortest contacts are clearly longer for **1(OH)ᴾᵗ·0.5MeOH** (3.336 Å) than for **1(NH₂)ᴾᵗ·0.5MeOH** (3.029 Å) (Fig. S16†) suggesting less steric repulsions for the former. As a result, the SCO becomes complete showing first the spin switch of Fe2 in two symmetric steps and later of Fe1 in a single step giving rise to a three-step spin transition. Obviously, the introduction of larger amounts of MeOH causes a gradual destabilization of the LS state of Fe1.

The water, methanol and ethanol adsorption studies carried out on **1(OH)ᴹ** and **1(NH₂)ᴹ** indicate that the replacement of the amine with the hydroxy group improves the uptake capacities of the network. Particularly, it enhances the affinity towards such guests since they are adsorbed more cooperatively and at higher rates by the hydroxy-substituted homologues. The structural analysis of these compounds shows that due to the better capacity of the hydroxy group to establish H-bonds, the host–guest interactions created in **1(OH)ᴹ** are noticeably stronger than those in **1(NH₂)ᴹ**, thus making the guest uptake energetically more favoured. Nevertheless, the adsorption mechanism inferred from the structural data is equivalent for both **1(OH)ᴹ** and **1(NH₂)ᴹ** compounds. It involves a series of structural modifications of the main network inducing the generation of 1D cavities along which the guests are located. These guest-induced structural transformations require a certain activation energy barrier which can be overcome through the interaction of the protic guest with the –OH or –NH₂ moieties. In this line, the stronger host–guest interactions established in **1(OH)ᴹ·xguest** seem to accelerate the crystal transformation required during the guest uptake enabling more effective and quantitative adsorptions. This initial energy barrier is also clearly reflected in the uptake of water, giving rise to a gate opening effect. This could be related to the rather hydrophobic character of the host structure which would explain the better affinity for the more hydrophobic guests MeOH and EtOH.[33] Nonetheless, the adsorption studies demonstrate that once the gate opening occurs and the 2D HCP adopts the open form, the smaller the size of the guest, the more cooperative the adsorption process. Besides, the enhanced adsorption cooperativity observed for water is likely due to the additional contacts established between these guests along the structural 1D channels (Fig. S3†).

Conclusions

The guest-dependent thermally-induced SCO of the unprecedented 2D Hofmann-like coordination polymers {Fe(5-OHPym)₂[M(CN)₄]}·guest (**1(OH)ᴹ·guest**, M = Pt, Pd; guest = H₂O, MeOH, EtOH) and their water, methanol and ethanol desorption/adsorption profiles have been presented. Both solvated and desolvated derivatives of these compounds are strictly isostructural to the previously reported **1(NH₂)ᴹ·guest**, only differing in axial ligand functionalization (hydroxy *vs.* amine groups). The structural flexibility displayed by **1(OH)ᴹ·guest** mirrors that of **1(NH₂)ᴹ·guest**, showing marked single-crystal to single-crystal transformations concomitant with the adsorption/desorption of small protic guests. The temperature dependent magnetic and calorimetric studies indicate that the desolvated species (**1(OH)ᴹ** and **1(NH₂)ᴹ**) show minimal differences in their complete one step SCO behaviours, thus suggesting a small effect of the OH/NH₂ exchange. In contrast, remarkable differences in the nature of the SCO (multistability) and transition temperatures (T_c) are observed between the solvated **1(OH)ᴹ·guest** and the **1**

$(NH_2)^M$·**guest** counterparts. Our structural data suggest that these differences arise from a combination of structural and inductive effects derived from the higher capacity of –OH to establish H-bond interactions. The same reason explains why the hydroxy-functionalized frameworks display a better affinity for small protic guests displaying more abrupt and quantitative adsorptions. This work highlights how very small compositional changes in a SCO framework can result in a significant enhancement of its adsorption properties and give access to a wide diversity of SCO behaviours. A deeper knowledge of the interplay between porosity and SCO in 2D HCPs would be considerably beneficial for their applications in chemical sensors and switching devices.

Conflicts of interest

There are no conflicts to declare.

Acknowledgements

Notes and references

1 O. Kahn and C. Jay-Martinez, Spin-Transition Polymers: From Molecular Materials Toward Memory Devices, *Science*, 1998, **279**, 44–48.

2 A. R. Pease, J. O. Jeppesen, J. F. Stoddart, Y. Luo, C. P. Collier and J. R. Heath, Switching Devices Based on Interlocked Molecules, *Acc. Chem. Res.*, 2001, **34**, 433–444.

3 J.-F. Létard, P. Guionneau and L. Goux-Capes, Towards Spin Crossover Applications, *Top. Curr. Chem.*, 2004, **235**, 221–249.

4 J. R. Heath, Molecular Electronics, *Annu. Rev. Mater. Res.*, 2009, **39**, 1–23.

5 M. D. Manrique-Juárez, S. Rat, L. Salmon, G. Molnár, C. M. Quintero, L. Nicu, H. J. Shepherd and A. Bousseksou, Switchable molecule-based materials for micro- and nanoscale actuating applications: Achievements and prospects, *Coord. Chem. Rev.*, 2016, **308**, 395–408.

6 E. Coronado, Molecular magnetism: from chemical design to spin control in molecules, materials and devices, *Nat. Rev. Mater.*, 2020, **5**, 87–104.

7 E. König, Nature and dynamics of the spin-state interconversion in metal complexes, *Struct. Bonding*, 1991, **76**, 51–152.

8 *Spin Crossover in Transition Metal Compounds Vol.: 233–235*, ed. P. Gütlich and H. A. Goodwin, Springer-Verlag, Berlin, 2004.

9 *Spin-Crossover Materials. Properties and Applications*, ed. M. A. Halcrow, John-Wiley & Sons, 2013.

10 P. Gütlich, A. Hauser and H. Spiering, Thermal and Optical Switching of Iron(II) Complexes, *Angew. Chem., Int. Ed. Engl.*, 1994, **33**, 2024–2054.

11 J. A. Real, A. B. Gaspar and M. C. Muñoz, Thermal, pressure and light switchable spin-crossover materials, *Dalton Trans.*, 2005, 2062–2079.

12 B. Weber, Spin crossover complexes with N_4O_2 coordination sphere—The influence of covalent linkers on cooperative interactions, *Coord. Chem. Rev.*, 2009, **253**, 2432–2449.

13 Y. Sunatsuki, R. Kawamoto, K. Fujita, H. Maruyama, T. Suzuki, H. Ishida, M. Kojima, S. Iijima and N. Matsumoto, Structures and spin states of mono- and dinuclear iron(II) complexes of imidazole-4-carbaldehyde azine and its derivatives, *Coord. Chem. Rev.*, 2010, **254**, 1871–1881.

14 G. Aromí, L. A. Barrios, O. Roubeau and P. Gamez, Triazoles and tetrazoles: Prime ligands to generate remarkable coordination materials, *Coord. Chem. Rev.*, 2011, **255**, 485–546.

15 R. W. Hogue, S. Singh and S. Brooker, Spin crossover in discrete polynuclear iron(II) complexes, *Chem. Soc. Rev.*, 2018, **47**, 7303–7338.

16 Y. Garcia, V. Niel, M. C. Muñoz and J. A. Real, Spin Crossover in 1D, 2D and 3D Polymeric Fe(II) Networks, *Top. Curr. Chem.*, 2004, **233**, 229–257.

17 J. A. Real, A. B. Gaspar, V. Niel and M. C. Muñoz, Communication between iron(II) building blocks in cooperative spin transition phenomena, *Coord. Chem. Rev.*, 2003, **236**, 121–141.

18 *Spin crossover phenomenon*, ed. A. Bousseksou, C. R. Chim., 2018, vol. 21, pp. 1055–1299.

19 M. Shatruk, H. Phan, B. A. Chrisostomo and A. Suleimenova, Symmetry-breaking structural phase transitions in spin crossover complexes, *Coord. Chem. Rev.*, 2015, **289–290**, 62–73.

20 N. Ortega-Villar, M. C. Muñoz and J. A. Real, Symmetry breaking in iron(II) spin-crossover molecular crystals, *Magnetochemistry*, 2016, **2**, 16–22.

21 M. C. Muñoz and J. A. Real, Thermo-, piezo-, photo- and chemo-switchable spin crossover iron(II)-metallocyanate based coordination polymers, *Coord. Chem. Rev.*, 2011, **255**, 2068–2093.

22 V. Rubio-Giménez, S. Tatay and C. Martí-Gastaldo, Electrical Conductivity and Magnetic Bistability in Metal–Organic Frameworks and Coordination Polymers: Charge Transport and Spin Crossover at the Nanoscale, *Chem. Soc. Rev.*, 2020, **49**(15), 5601–5638.

23 Z.-P. Ni, J.-L. Liu, M. N. Hoque, W. Liu, J.-Y. Li, Y.-C. Chen and M.-L. Tong, Recent advances in guest effects on spin-

crossover behaviour in Hofmann-type metal-organic frameworks, *Coord. Chem. Rev.*, 2017, **335**, 28–43.

24 (*a*) T. Kosone, R. Kosuge, M. Tanaka, T. Kawasaki and N. Adachi, New family of Hofmann-like coordination polymers constructed with imidazole ligands and associated with spin crossover and anisotropic thermal expansions, *New J. Chem.*, 2022, **46**, 10540–10544; (*b*) K. A. Zenere, S. G. Duyker, E. Trzop, E. Collet, B. Chan, P. W. Doheny, C. J. Kepert and S. M. Neville, Increasing spin crossover cooperativity in 2D Hofmann-type materials with guest molecule removal, *Chem. Sci.*, 2018, **9**, 5623–562; (*c*) E. Milin, V. Patinec, S. Triki, E. E. Bendeif, S. Pillet, M. Marchivie, G. Chastanet and K. Boukheddaden, Elastic Frustration Triggering Photoinduced Hidden Hysteresis and Multistability in a Two-Dimensional Photoswitchable Hofmann-Like Spin-Crossover Metal–Organic Framework, *Inorg. Chem.*, 2016, **55**, 11652–11661; (*d*) Y. M. Klein, N. F. Sciortino, F. Ragon, C. E. Housecroft, C. J. Kepert and S. M. Neville, Spin crossover intermediate plateau stabilization in a flexible 2-D Hofmann-type coordination polymer, *Chem. Commun.*, 2014, **50**, 3838–3840.

25 R. Ohtani and S. Hayami, Guest-Dependent Spin-Transition Behavior of Porous Coordination Polymers, *Chem. – Eur. J.*, 2017, **23**(10), 2236–2248.

26 B. Kumar, A. Paul, D. J. Mondal, P. Paliwal and S. Konar, Spin-State Modulation in Fe^{II}-Based Hofmann-Type Coordination Polymers: From Molecules to Materials, *Chem. Rec.*, 2022, e202200135.

27 J.-P. Xue, Y. Hu, B. Zhao, Z.-K. Liu, J. Xie, Z.-S. Yao and J. Tao, A spin-crossover framework endowed with pore-adjustable behavior by slow structural dynamics, *Nat. Commun.*, 2022, **13**, 3510–3520.

28 F.-L. Liu and J. Tao, Hysteretic Two-Step Spin-Crossover Behavior in Two Two-Dimensional Hofmann-Type Coordination Polymers, *Chem. – Eur. J.*, 2017, **23**, 18252–18257.

29 R. Turo-Cortés, M. Meneses-Sánchez, T. Delgado, C. Bartual-Murgui, M. C. Muñoz and J. A. Real, Coexistence of luminescence and spin-crossover in 2D iron(II) Hofmann clathrates modulated through guest encapsulation, *J. Mater. Chem. C*, 2022, **10**, 10686–10698.

30 R. Turo-Cortés, C. Bartual-Murgui, J. Castells-Gil, M. C. Muñoz, C. Martí-Gastaldo and J. A. Real, Reversible guest-induced gate-opening with multiplex spin crossover responses in two-dimensional Hofmann clathrates, *Chem. Sci.*, 2020, **11**, 11224–11234.

31 Θ is defined as $\sum_{i=1}^{24} (60 - \theta_i)$, θ_i being the angle generated by superposition of two opposite faces of the octahedron (there are four pairs of such superpositions with six θ values for each). Σ represents octahedral distortion defined as the sum of deviations from 90° of the 12 *cis* N–Fe–N angles in the coordination sphere $\sum_{i=1}^{12} |\varphi_i - 90|$.

32 P. Gilli, L. Pretto, V. Bertolasi and G. Gilli, Predicting Hydrogen-Bond Strengths from Acid-Base Molecular Properties. The pKa Slide Rule: Toward the Solution of a Long-Lasting Problem, *Acc. Chem. Res.*, 2009, **42**, 33–44.

33 S. Horike, D. Tanaka, K. Nakagawa and S. Kitagawa, Selective guest sorption in an interdigitated porous framework with hydrophobic pore surfaces, *Chem. Commun.*, 2007, 3395–3397.

This journal is © the Partner Organisations 2023

Inorg. Chem. Front., 2023, **10**, 600–611 | **611**